# Drivers for mass and momentum exchange between the main channel and river bank lateral cavities

Ouro, Pablo; Juez, Carmelo; Franca, Mário

**DOI**
10.1016/j.advwatres.2020.103511

**Publication date**
2020

**Document Version**
Final published version

**Published in**
Advances in Water Resources

Advances in Water Resources 137 (2020) 103511

Contents lists available at ScienceDirect

Advances in Water Resources

journal homepage: www.elsevier.com/locate/advwatres

# Drivers for mass and momentum exchange between the main channel and river bank lateral cavities

Pablo Ouro [a,*], Carmelo Juez [b], Mário Franca [c,d]

[a] Hydro-environmental Research Centre, School of Engineering, Cardiff University The Parade CF24 3AA, Cardiff, United Kingdom
[b] Instituto Pirenaico de Ecología, Consejo Superior de Investigaciones Científicas (IPE-CSIC), Campus de Aula Dei, Avenida Montañana 1005, Zaragoza 50059, Spain
[c] IHE-Delft Institute for Water Education, Delft, The Netherlands
[d] Department of Hydraulic Engineering, Delft University of Technology, Delft, The Netherlands

ARTICLE INFO

*Keywords:*
Large-Eddy Simulation
Turbulence
Open channel flow
Mass transport
Hydrodynamics
River bank embayments

ABSTRACT

Large-Eddy Simulations (LES) are used to investigate the governing processes involved in mass and momentum transfer between the flow in the main channel and symmetrically-distributed lateral bank cavities. In-cavity free-surface velocities, based on laboratory measurements made in an open channel, are used to validate the numerical results. A main vortical structure dominates the in-cavity flow which, despite the shallow nature of the flow, features a remarked three dimensional dynamics. LES results outline the largest velocities through the mouth of the cavity are attained in two thin regions near the bottom-bed and free-surface. In the shear layers established between the main channel and cavities is where the main transfer of turbulent momentum is made between these two flow regions, and the numerical simulations capture well the instantaneous coherent flow structures, e.g. Kelvin-Helmholtz vortices. LES captures a low-frequency standing wave phenomenon even with a rigid-lid approximation adopted at the free-surface boundary. Momentum exchange between cavities and main channel is analysed using the Reynolds Averaged momentum equation in the transverse direction, revealing that the pressure gradient term is the unique contributor to flushing momentum out of the cavities whilst convection and Reynolds normal stress terms are responsible for its entraining into the cavity. Furthermore, sediment deposition areas documented in the laboratory experiments are linked with the simulated hydrodynamics, which correlate with regions of low turbulent kinetic energy and vertical velocities near the bottom of the channel. Overall, the results shed new light into the complex mechanisms involved in mass and momentum transfer; this will aid to design embayments more efficiently regarding sediment transport processes.

## 1. Introduction

Lateral embayments or cavities are often present in natural or human-influenced rivers. In natural rivers these typically constitute areas of sediment accumulation and flow velocity diversity, making these areas ecology hotspots within the fluvial network and controls of the river basin distribution of water and sediments. Artificial lateral cavities or local widening are often implemented in channelised rivers as nature-inspired river restoration measures. Anthropologically altered rivers have typically uniform cross sections and monotonous river banks, which contrast with natural river channels where large-scale and diversified flow and morphology can be found. This hinders the development of fish and vegetation habitats that require areas with differentiated flow velocities (Wood and Armitage, 1997; Kemp et al., 2011). With the intention to foster new flow patterns that diversify the velocity fields and promote the accumulation of sediment and sheltering conditions for aquatic biota, local widening establishing lateral embayments or cavities is a common practice in restoration projects mimicking natural conditions. The so-called Wandos in Japan are built to enable areas for fish spawning and nursery (Uno et al., 2013; Nezu and Onitsuka, 2002) and (Ribi et al., 2014) showed the suitability of lateral embayments to provide shelter to fish. Harbors in rivers may be conceptualised as cavities lateral to the flow in the main channel, and these may be subjected to siltation of material transported in the main stream (Langendoen et al., 1994; van Schijndel and Kranenburg, 1998). Finally, lateral embayments may be artificially created to capture fine sediments and thus maintain a central navigable channel, as in the historical case of the *casiers de Girardon* in the lower-Rhône (France) (Thorel et al., 2018).

A thorough design of the geometry of such local widenings in a river reach is needed in terms of their impact on the channel hydrodynamics (Valentine and Wood, 1979; Uijttewaal et al., 2001; Weitbrecht et al., 2008; Lesack and Marsh, 2010; Sukhodolov, 2014; Akutina, 2015; Mignot et al., 2017; Navas-Montilla et al., 2019) and on the transport of

* Corresponding author.
*E-mail addresses:* ourop@cardiff.ac.uk (P. Ouro), carmelo.juez@ipe.csic.es (C. Juez), m.franca@un-ihe.org (M. Franca).

https://doi.org/10.1016/j.advwatres.2020.103511
Received 26 September 2019; Received in revised form 16 December 2019; Accepted 15 January 2020
Available online 15 January 2020

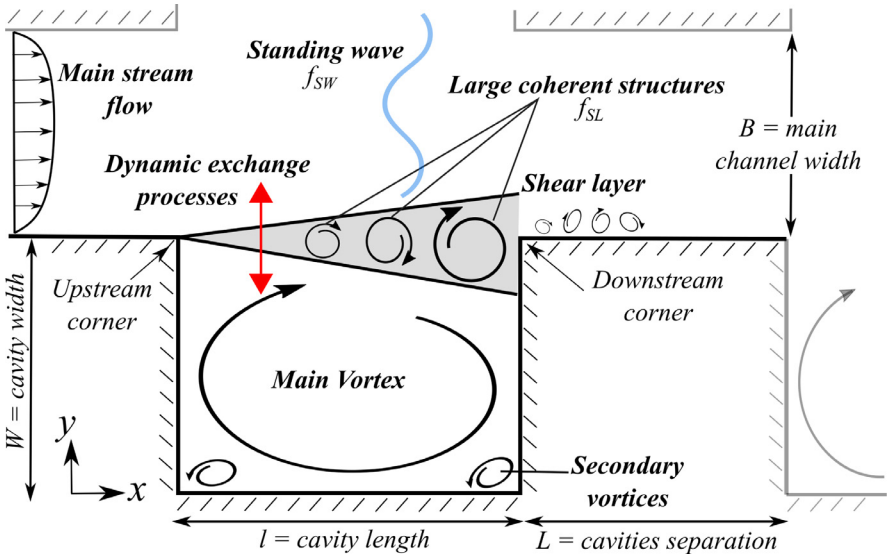


**Fig. 1.** Schematic of the flow phenomena typically present in the hydrodynamics of lateral bank cavities. The lateral cavities are characterised by the cavity length $l$, the distance between two cavities $L$ and the lateral width of the cavities $W$.

such environmental variables as fine sediments (Juez et al., 2018a; Juez et al., 2018c), pollutants, oxygen and nutrients (Jackson et al., 2012; Jackson et al., 2013; Sanjou et al., 2018). As a result, numerous field, laboratory and numerical studies were carried out to elucidate the mass and momentum exchange mechanisms between the main flow and the lateral cavities.

Traditionally, it has been common to derive mass and momentum fluxes from the flow patterns observed on the water surface of laboratory experiments and in the field. However, this approach based on the superficial flow features over-simplifies the complexity of these flows and ignore the possible three-dimensional (3D) nature of the exchange processes observed in the interaction between the main flow and lateral embayments. Conceived from the existing knowledge in the literature, Fig. 1 presents a conceptual model of open-channel flow when lateral embayments perpendicular to the main flow are present, which includes: a main recirculating vortex inside the cavity occupying most of its volume; vertically-oriented coherent structures which are shed from the shear layer with a frequency $f_{SL}$; secondary low-energetic vortices in the internal corners of the cavity; and standing resonant waves that appear due to the enclosed water domain (also called seiches, Kimura and Hosoda, 1997) oscillating at a frequency $f_{SW}$ in the cross-flow direction and causing important pressure fluctuations.

Transport and settling of sediments in open channel flow can vary depending on the flow conditions, cross-section, channel aspect ratio or physical properties of the sediments, among others. Nikora and Goring (2002) evidenced that turbulence is a key factor in sediment transport flux, which is often neglected and sediment flux is often associated solely to the mean flow, and that phenomena such as turbulent bursting events are temporally well correlated with sediment transport processes. A larger degree of complexity arises in curved channels or when lateral embayments perpendicular to the main flow are found.

Juez et al. (2018a) carried out systematic laboratory experiments in an open channel, with a large number of different geometries of lateral embayments in the channel banks, to investigate the interplay between flow hydrodynamics and the transport (under suspension) and accumulation of fine sediments. The in-cavity sedimentation pattern for several combinations of geometrical configurations and flow conditions were analysed under a two-dimensional framework. However, the results pointed out the existence of 3D flow features which relate the location and magnitude of the in-cavity flow patterns with sedimentation patterns and amount of fine sediment trapped. In their studies, Juez et al. (2018a,b) observed evidences that the three-dimensionality of the flow was non-negligible, especially for the less shallow flow conditions, which did not allow to fully elucidate the direct link between the flow and the sediment transport processes.

To unravel the details of such complex flow, high-fidelity detailed numerical simulation tools were used. Both Detached-Eddy Simulations (DES) and Large-Eddy Simulations (LES) are techniques that aid to understand the hydrodynamics of multi-scale turbulent flow structures under the presence of groynes and lateral embayments (McCoy et al., 2008; Constantinescu et al., 2009; Fang et al., 2014). These computational approaches, if equipped with the necessary high spatial resolution, can accurately resolve the dominant quasi-2D flow structures, e.g. large-scale energetic or shear-layer vortices, and also smaller 3D vortices. DES or LES not just provide the required resolution of the turbulent structures but they can accurately predict areas of flow separation of high importance in open channel and river flows, proving their superiority to Reynolds Averaged Navier-Stokes (RANS) computations (van Balen et al., 2010; Juez et al., 2014; Navas-Montilla and Murillo, 2016). Thus, these eddy-resolving techniques provide valuable and complete information of the turbulent flow dynamics (Ouro et al., 2018a), which ultimately, govern mass and momentum exchange processes (McCoy et al., 2006; Gualtieri, 2008).

This paper conducted numerical simulations by means of LES to reveal 3D flow hydrodynamics (i.e. mass/momentum fluxes and turbulent structures) in lateral embayments of open-channel flows. The numerical results contribute to determine the underlying physical mechanisms for mass and momentum transfer between the main channel and the lateral embayments as well as evidencing the feasibility of considering the flow shallowness (2D nature). Ultimately, these outcomes are related to the sediment erosion/transport processes observed in the laboratory experiments by Juez et al. (2018b). Furthermore, the identification of preferential regions for mass and momentum transfer across the opening of the cavities is possible through the results of the numerical simulations. This is essential information in what concerns the design of lateral embayments either to function as river restoration measures, as fluvial harbours or as sediment traps to keep main channels navigable. The present study focuses on one geometrical configuration experimentally tested by Juez et al., 2018a with three different flow discharges. This geometrical configuration was chosen from others previously investigated, since it corresponded to sedimentation patterns which contained flow diversity and morphology, hence ideal as nature-inspired solution for river restoration. The numerical simulations herein outlined adopt the large-eddy simulation approach to resolve the governing equations using the in-house code Hydro3D (Ouro et al., 2019). Despite these large-eddy simulations do not explicitely consider sediment transport, the hydro-

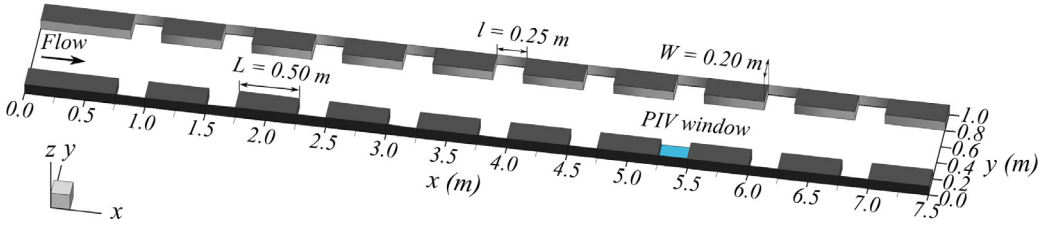


**Fig. 2.** Representation of the channel configuration tested in (Juez et al., 2018a), including the relevant geometric dimensions. The cavity in which PIV measurements were taken is highlighted in blue. (For interpretation of the references to color in this figure legend, the reader is referred to the web version of this article.)

**Table 1**
Hydrodynamic conditions of the configurations studied.

| Case | $Q$ [l/s] | $h$ [m] | $U_0$ [m/s] | $Re$ [-] | $Fr$ [-] |
|---|---|---|---|---|---|
| Q1 | 4.8 | 0.035 | 0.227 | 28,487 | 0.39 |
| Q2 | 8.5 | 0.050 | 0.295 | 50,568 | 0.42 |
| Q3 | 15.0 | 0.070 | 0.355 | 80,645 | 0.43 |

dynamic results serve as a proxy to link the flow fluxes to the observed sediment transport pathways.

## 2. Laboratory experiments and numerical simulations

### 2.1. Laboratory setup

Experiments were carried out in a channel which works in a closed circuit with the following components (see Juez et al., 2018a; Juez et al., 2018c for a more detailed description): (i) an upstream 2 m long, 1 m wide and 1 m high tank for mixing suspended sediments, (ii) a rectangular 7.5 m long, 1.0 m wide and 1.0 m high open-channel with 0.1% slope, and (iii) a downstream tank of 3.5 m long, 1 m wide and 1 m high that collects the water and sediments for recirculation. The water is pumped from the downstream to the upstream tank through a pipe system equipped with a valve to control the discharge and a flow meter. The channel bottom is smooth and made of painted wood. Upstream, the transition between the head tank and the channel reach is made by a honeycomb-type flow tranquilliser. Downstream from the channel, a Venetian gate allows the flow depth to be controlled. The base channel banks were modified by placing concrete bricks by the lateral walls. This allowed to build lateral embayments in the laboratory channel (see Fig. 2).

Two-dimensional (2D) surface velocity fields in the lateral embayments were measured by means of surface PIV technique. Therefore, instantaneous ($u$, $v$), mean ($U$, $V$) and fluctuating ($u'$, $v'$) values for the streamwise and spanwise velocities were recorded at the water surface. The water level was recorded all through the experiments by an ultrasonic probe.

Uniform fine sediment with a $d_{50} = 0.2$ mm was supplied in the upstream tank of the channel at the beginning of each test. The mean diameter of the fine sediment particles was representative of the Rhône river (Federal Office of Environment, 2016). Sediments were trapped inside the lateral cavities. At the end of the experiments, the sediment deposits inside the cavities were photographed. The obtained photos were treated to determine the area occupied by the settled sediments.

The lateral embayments configuration studied in this work corresponds to geometrical configuration 2.1 in Juez et al., 2018a, i.e. 0.25 m long ($l$) and 0.20 m wide ($W$) cavities with a streamwise spacing between consecutive cavities ($L$) of 0.40 m. The main channel width ($B$) is 0.60 m. Three different discharges were tested experimentally, which correspond to different values of the ratio between the water height, $h$, and the channel width, $b$: $b/h = 17.26 - 7.20$; i.e. from more to less shallow uniform flow conditions. Table 1 displays the main flow characteristics of the experiments herein studied, namely flow discharge ($Q$), water depth ($h$), bulk velocity ($U_0$), bulk Reynolds number ($Re = hU_0/\nu$, where $\nu$ is the water kinematic viscosity), and Froude number ($Fr = U_0/(gh)^{1/2}$, where $g$ stands for the gravity acceleration).

### 2.2. Numerical framework

High-fidelity numerical simulations are performed using the in-house code Hydro3D (Ouro et al., 2018b), which resolves the flow dynamics by means of Large-Eddy Simulation (LES) (Liu et al., 2017; Ouro et al., 2018a; Ouro et al., 2017; Stoesser, 2010; Stoesser et al., 2008). In the framework of LES, the flow structures larger than a given filter size, e.g. grid spacing, are explicitly resolved whilst those smaller are modelled (Rodi et al., 2013). Hence, the governing equations in LES are the spatially-filtered mass and momentum conservation Navier-Stokes equations for incompressible viscous flow that read as:

$$\frac{\partial u_i}{\partial x_i} = 0 \tag{1}$$

$$\frac{\partial u_i}{\partial t} = -\frac{1}{\rho}\frac{\partial p}{\partial x_i} - \frac{\partial u_i u_j}{\partial x_j} + \nu\frac{\partial^2 u_i}{\partial x_j^2} - \frac{\partial \tau_{ij}}{\partial x_j} + \frac{1}{\rho}\frac{\partial p_0}{\partial x_i}\delta_{11} \tag{2}$$

Here $u_i$ and $x_i$ are the vectors of velocities and coordinates, $p$ denotes pressure, $\nu$ and $\rho$ are the kinematic viscosity and density of the fluid respectively, $\tau_{ij}$ represents the sub-grid scale stresses, and $\delta$ is the Kronecker delta. Periodic streamwise flow condition ($x_1$) is adopted with a constant pressure gradient $p_0$, which ensures uniform flow rate $Q$, applied only to the main channel region, i.e. not applied to the lateral cavities region (Bomminayuni and Stoesser, 2011).

In Hydro3D, the computational domain is discretised as a rectangular Cartesian mesh divided into smaller sub-domains which are intercommunicated via Message Passing Interface (MPI) to perform the simulation in parallel (Ouro et al., 2019). Staggered storage arrangement of velocities is adopted with fourth-order central differences to approximate velocity fluxes and the Poisson pressure equation is solved using a multi-grid technique (Cevheri et al., 2016). The simulation is advanced in time using a fractional-step method with a three-step Runge-Kutta method providing a second order accuracy in time. The Wall-Adapting Local-Eddy viscosity model from Nicoud and Ducros (1999) is used to calculate the sub-grid scale stress tensor.

The computational domain spans 1.5 m long ($x/l = 6$) and comprises two cavities on each lateral boundary of the channel, as depicted in Fig. 3. The simulations start with an initial uniform velocity field and run for several flow-throughs using inflow-outflow conditions to allow the flow to develop within the cavities and remove any transients in the main channel from the initial flow state. Thereafter, periodic streamwise conditions are applied, which represents a scenario of an infinite array of lateral cavities. At the bottom and lateral walls, a non-slip condition is imposed as the first computational grid cell is within the viscous sublayer. The free-surface is treated as a shear-free rigid lid as the Froude numbers of the studied cases are below 0.5 (Constantinescu et al., 2009; Koken and Constanstinescu, 2009). Seiching across the channel was not

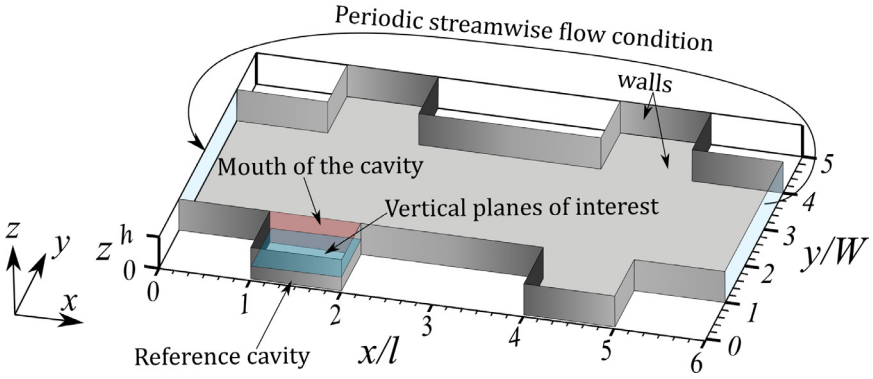


**Fig. 3.** Geometric configuration of the computational domain which corresponds to configuration 2.1 in the laboratory work of Juez et al. (2018a). Given the symmetrical and periodical characteristics of the physical system, two lateral embayments on each side were used when building the computational domain. A periodic streamwise flow condition is imposed in the main channel upstream and downstream ends.

**Table 2**
Details of the grid resolution in streamwise ($\Delta x$) and vertical ($\Delta z$) directions, vertical resolution in wall units ($\Delta z^+$), friction velocity ($u_*$) obtained from experiments and LES, and eddy turn-over time ($t_e = h/u_*$), for the flow configurations studied.

| Case | $\Delta x$ [m] | $\Delta z$ [m] | $\Delta z^+$ [-] | $u_*$ (LES) [m/s] | $u_*$ (Exp) [m/s] | $t_e$ [s] |
|---|---|---|---|---|---|---|
| Q1 | 0.0010 | 0.0010 | 6.91 | 0.014 | 0.018 | 2.53 |
| Q2 | 0.0010 | 0.0010 | 8.73 | 0.017 | 0.021 | 2.86 |
| Q3 | 0.0010 | 0.0005 | 5.06 | 0.020 | 0.024 | 3.46 |

observed during the experiments for the selected geometrical configuration herein chosen (Juez et al., 2018c).

The resolution of the numerical grids is uniform across the whole domain and details are provided in Table 2. For the two lowest discharges (Q1 and Q2) the grid size is 1 mm, whilst for Q3 the same resolution is used in $x$- and $y$-direction and that in the vertical increases to 0.5 mm, as the increase in friction velocity due to higher flow discharge requires higher resolution to have the first grid off the wall within the viscous sub-layer ($\Delta z^+ = \Delta z u_*/\nu < 12$, Rodi et al. (2013)). The meshes comprise a total of 38.5, 55 and 154 million elements for the different cases and the simulations run using between 100 and 300 CPUs on *Supercomputing Wales* facilities.

For the time integration in the LESs, variable time step is adopted with constant Courant-Friedrichs-Lewy (CFL) value equal to 0.3 in order to guarantee numerical stability. As the bulk conditions of the three study cases are different, the simulations run for an approximately equivalent physical time of 190 eddy turn-over time, defined as $t_e = h/u_*$, representative of the time-scale of the largest flow structures in the main channel. This criterion yields to a total simulation times of 559 s, 620 s and 680 s in cases Q1, Q2 and Q3, respectively. These time integration intervals are long enough to ensure converged flow statistics. The LES-computed friction velocity presented in Table 2 is obtained from the time-averaged pressure gradient as $u_* = \sqrt{dp/dx \mathrm{R}_h/\rho}$, where $\mathrm{R}_h$ stands as the main-channel hydraulic radius and $dp/dx$ is the time-averaged pressure gradient imposed in the main channel to keep a constant flow rate $Q$. LES consistently underpredicts the friction velocity by approximately 15% compared to the experimental value. This may be attributed to the lack of modelling the concrete rough walls or representing an infinite array of lateral embayments using periodic boundary conditions, which might lead to slightly different flow conditions from those found in the experiments at the measured location.

The analysis of the transport of momentum across the cavity opening is analysed using the LES results, evaluated with the contribution of each terms of the Reynolds-averaged momentum equation in $y$-direction, in which steady conditions are assumed, i.e. $\partial V/\partial t = 0$. The adopted Reynolds-Averaged Navier-Stokes (RANS) equation in $y$-direction reads:

$$0 = \underbrace{-U\frac{\partial V}{\partial x}}_{\mathrm{I}} \underbrace{-V\frac{\partial V}{\partial y}}_{\mathrm{II}} \underbrace{-W\frac{\partial V}{\partial z}}_{\mathrm{III}} \underbrace{-\frac{\partial u'v'}{\partial x}}_{\mathrm{IV}} \underbrace{-\frac{\partial v'v'}{\partial y}}_{\mathrm{V}} \underbrace{-\frac{\partial v'w'}{\partial z}}_{\mathrm{VI}} \underbrace{-\frac{1}{\rho}\frac{\partial P}{\partial y}}_{\mathrm{VII}} \underbrace{+\nu\left(\frac{\partial^2 U}{\partial x^2}+\frac{\partial^2 V}{\partial y^2}+\frac{\partial^2 W}{\partial z^2}\right)}_{\mathrm{VIII}} \quad (3)$$

Here the terms I, II and III represent the convective transport of y-axis momentum, the momentum transport due to turbulent stresses correspond to the terms IV to VI, term VII is the pressure gradient that drives the flow into the cavity, and term VIII corresponds to the viscous stresses.

## 3. Results

### 3.1. Time-averaged flow

Time-averaged flow field developed in the reference cavity and in the adjacent area of the main channel is presented in Fig. 4 for the horizontal plane at $z/h = 0.5$. Contours of mean streamwise (a) and transverse (b) velocities, streamwise (c) and transverse (d) turbulence intensities, Reynolds shear stress $u'v'$ (e) and turbulent kinetic energy (defined as $tke = u_i' u_i'/2$) (f), are shown for the flow conditions corresponding to case Q2. Results are adimensionalised using the bulk velocity of the main channel, $U_0$, and shear velocity, $u_*$.

Flow streamlines reveal that a single recirculating vortex (hereinafter denoted as Main Vortex (MV)) is formed within each cavity occupying most of its volume governing the in-cavity flow, whilst secondary vortical structures of much smaller size are generated at the corners, forced by continuity and the no-slip condition at the cavity walls. These can be deemed to have negligible influence on the hydrodynamics (Mignot et al., 2017). Maximum streamwise negative velocities are found near the wall opposite to the cavity opening, reaching values up to $U \approx -0.25U_0$. The in-cavity flow observed corresponds to the skimming flow type due to its geometric aspect ratio near the unity (Meile et al., 2011). In such flow type, the recirculating MV is largely decoupled from the main stream flow and no interference between cavities happens, which can be translated into reduced mass and momentum exchange. Furthermore, typically if the aspect ratio is from 0.5 to 1.5, one single eddy is observed in the cavity.

Areas of large velocity fluctuations reveal high turbulence activity and second-order statistics are observed to be maximum across the shear layer generated between the cavities and the main channel, i.e. $y/l = 0.8$, with nevertheless some degree of penetration into the cavity near the downstream inner wall. In the contribution to turbulent kinetic energy, $u'$ values are found larger than $v'$ across the mouth of the cavity even though momentum exchange between main stream and cavities seems

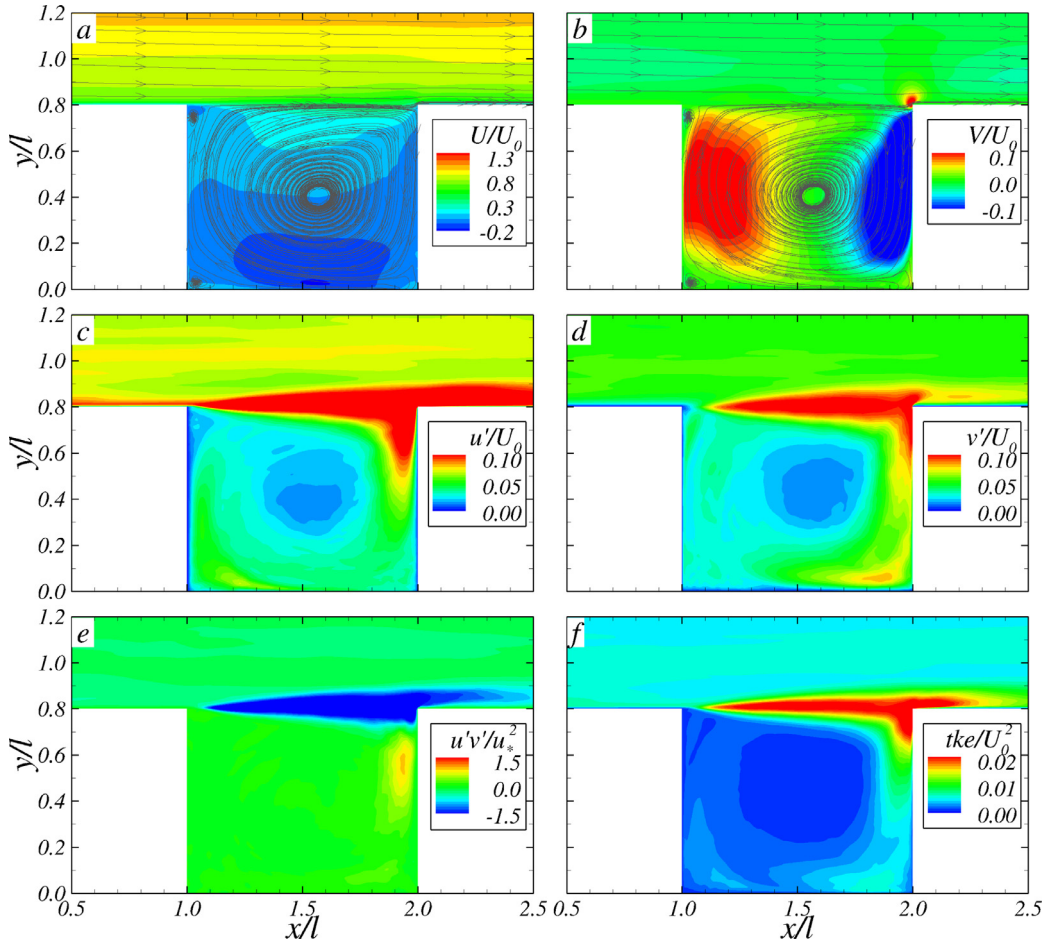


**Fig. 4.** Distribution of normalised time-averaged (a) streamwise ($U/U_0$) and (b) transverse velocities ($V/U_0$), (c) streamwise ($u'/U_0$) and (d) transverse ($v'/U_0$) turbulence intensities, (e) Reynolds shear stress ($u'v'/u_*^2$), and (f) turbulence kinetic energy ($tke/U_0^2$), for the case Q2 and for the horizontal plane at $z/h = 0.5$. Flow streamlines are only drawn in a and b for sake of simplicity.

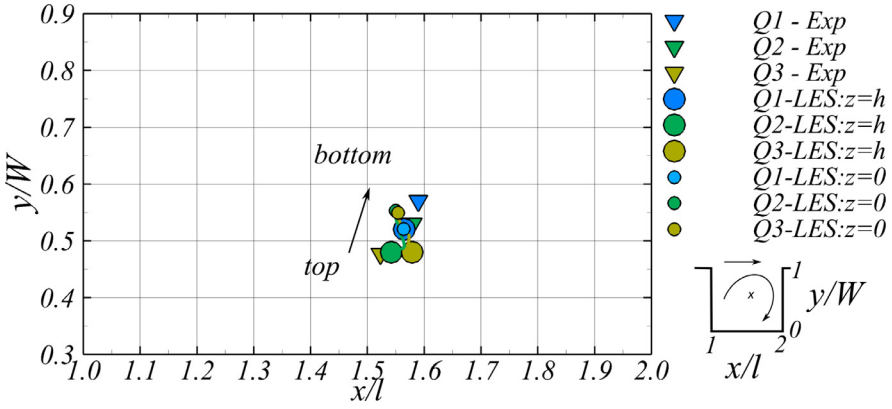


**Fig. 5.** Zoom-in of the location of the recirculating main vortex core position obtained from time-averaged velocities computed with LES and experimental measurements from Juez et al. (2018a).

to be predominantly in the transverse direction. Regions of large $u'$ are also observed across the main channel lateral wall at downstream of the cavities. These fluctuation of streamwise velocities are due to the coherent structures recurrently shed in the shear-layer as depicted in Fig. 1 and presented later in Section 3.2. Inside the cavity, minima of velocity fluctuations are attained close to the core of the recirculating MV suggesting that this is mostly stationary in time without major spatial oscillations across the cavity region, as commonly found in skimming flows (Weitbrecht et al., 2008). Contours of Reynolds shear stress reveal the shear layer grows in size since the upstream outer corner and reaches its widest distribution close to the downstream cavity corner (Mignot et al., 2017).

A key aspect in the simulation of embayment flows is the prediction of the position of the core of the recirculating main vortex, MV, since this is somewhat related to the sedimentation patterns which are observed in the cavity bottom. Fig. 5 presents the relative coordinates ($x/l$, $y/W$) of the recirculating vortex core for two extreme positions in the water column, i.e. water surface ($z = h$) and cavity bottom ($z = 0$). These positions were determined based on the streamlines of mean flow from LES (e.g. Fig. 4a). In the same figure, the position of the MV core

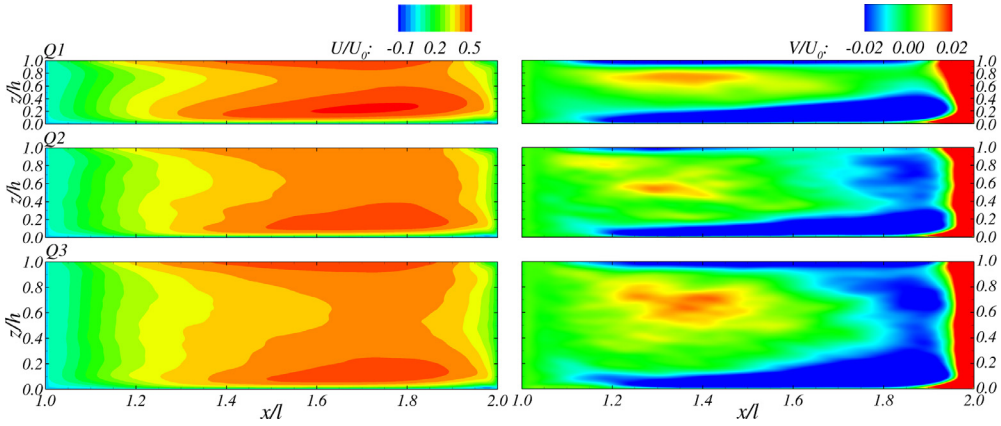


**Fig. 6.** Distribution at a plane through the mouth of the cavity at $y/W = 1.0$ (cf. Fig. 3) of the normalised time-averaged streamwise ($U/U_0$) and transverse ($V/U_0$) velocities for the three cases.

for the surface observations made in the experimental work with surface PIV (Juez et al., 2018a) are represented as well.

The 3D nature of this vortical structure is obvious confirming the results by Tuna et al. (2013): the superficial position of the main vortex does not match the position of the core of the vortex close to the bottom. Taking into account the vertical variation, for case Q1, the shift in the core position is small. On the contrary, for the two higher discharges and water depths (Q2 and Q3), the vortex centre moves towards the mouth of the cavity with increasing submergence. The largest change in the core position is observed for the highest Reynolds number case, i.e. Q3. A trend with the flow is observed for both the numerical and laboratory results: when becoming shallower, the core of the vortical structure approaches the cavity entrance. Overall, a good agreement is found between computational and experimental data, with the LES predicting the $x$-locations within a 4% error margin and within a 10% accuracy for $y-$coordinates.

The distribution of the mean flow across the transition plane between the main stream and the lateral cavity is presented in Fig. 6 for the three cases withh contours of streamwise and transverse velocities. A similar pattern of $U/U_0$ is developed in cases Q2 and Q3, in which the largest velocities are found in the downstream half with maximum values attained near the bottom and at the free-surface. In case Q1 there seems to exist a more uniform distribution of the maximum velocity through the channel-cavity transitions section, which is a consequence of shallowness.

The spatial region of maximum negative cross-flow velocities $V/U_0$ appears to be similar among cases, specifically at $1.2 < x/l < 1.9$, at $z/h \approx 0.3$ for Q2 and Q3, whilst for Q1 a slightly higher position is found of $z/h \approx 0.4$. The cross-flow mean velocity $V$ is the main responsible for exchange of mass and momentum between the cavities and the main channel by the mean flow. The negative $V$-velocity areas identify where mass entrains into the cavity (Sanjou and Nezu, 2013). Conversely, mass flush out mainly occurs at two locations, across the entire water depth near the downstream cavity wall at $x/l > 1.9$ and, with lower velocity values, between $0.2 < z/h < 0.9$ in the upstream half of the cavity mouth section. Note that for cases Q2 and Q3, in the region of $1.8 < x/l < 1.9$, entraining flow is found across the water column while this is not observed in the case with the lowest discharge.

Fig. 7 shows second-order flow statistics, only for case Q2 for the sake of brevity. The mostly 2D distribution of the three components of turbulence intensity and turbulent kinetic energy reveal that the flow near the upstream corner of the cavity is less turbulent while, after a distance of $x/l = 1.2$, the turbulence activity in this pane grows. Lower levels of turbulence are observed near the channel bed and free-surface. Contours of Reynolds shear stresses $u'v'$ along the mouth of the cavity feature negative values with an almost uniform distribution in the vertical direction. The growing turbulence activity from the upstream

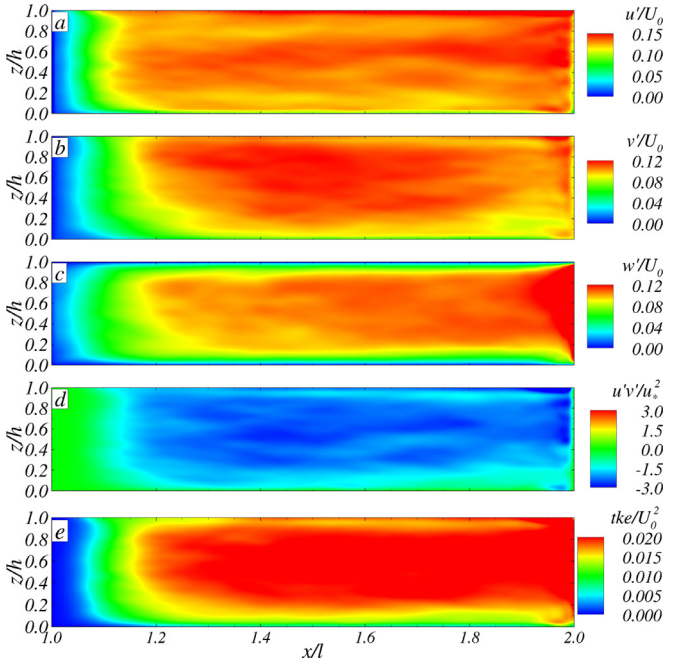


**Fig. 7.** Distribution at a plane through the mouth of the cavity at $y/W = 1.0$ (cf. Fig. 3) of the (a) streamwise ($u'/U_0$), (b) transverse ($v'/U_0$) and (c) vertical ($w'/U_0$) turbulence intensities, (d) Reynolds shear stress ($u'v'/u_*^2$) and (e) $tke/U_0^2$, for the case Q2.

towards the downstream cavity wall is in agreement with the development of the shear layer sketched in Fig. 1 and visible in Fig. 4, which is the expected main region of turbulence production in this flow.

Qualitative comparison of velocities at the free-surface layer between LES and experiments is presented in Fig. 8, with profiles of $U/U_0$ and $V/U_0$ along transverse locations $x/l = 1.25$ and 1.50 for the three cases. Distribution of $U$ shows that negative velocities are found for $y/W < 0.5$ for most cases, as expected from the contours of $U$ in Fig. 4a. While in the mid region of the cavity LES agrees well with the PIV data, discrepancies are observed near the wall opposite to the mouth of the cavity, i.e. $y/W = 0.0$. This is attributed to the known difficulty for the 2D-PIV to provide accurate velocity estimates near the walls, due to the decreasing concentration of tracer particles and strong flow gradients near the walls, these velocity measurements are usually biased (Kähler et al., 2012). Profiles of transverse velocity show nevertheless a good match between computational and experimental data at both locations for all the studied cases.

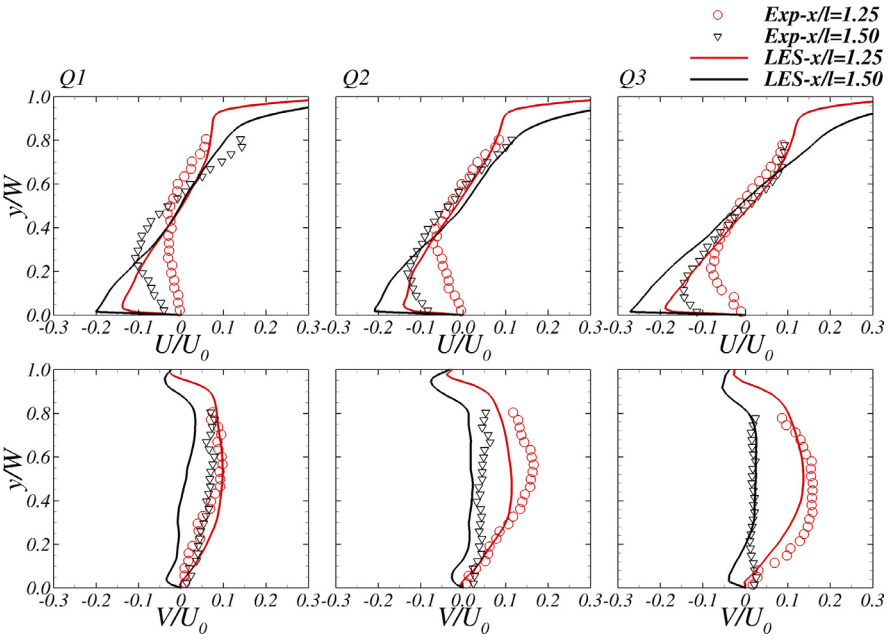


**Fig. 8.** Transverse profiles of streamwise ($U/U_0$) and transversal ($V/U_0$) velocities at $x/l = 1.25$ and 1.50. Comparison between experiments (Juez et al., 2018a) and present LES results.

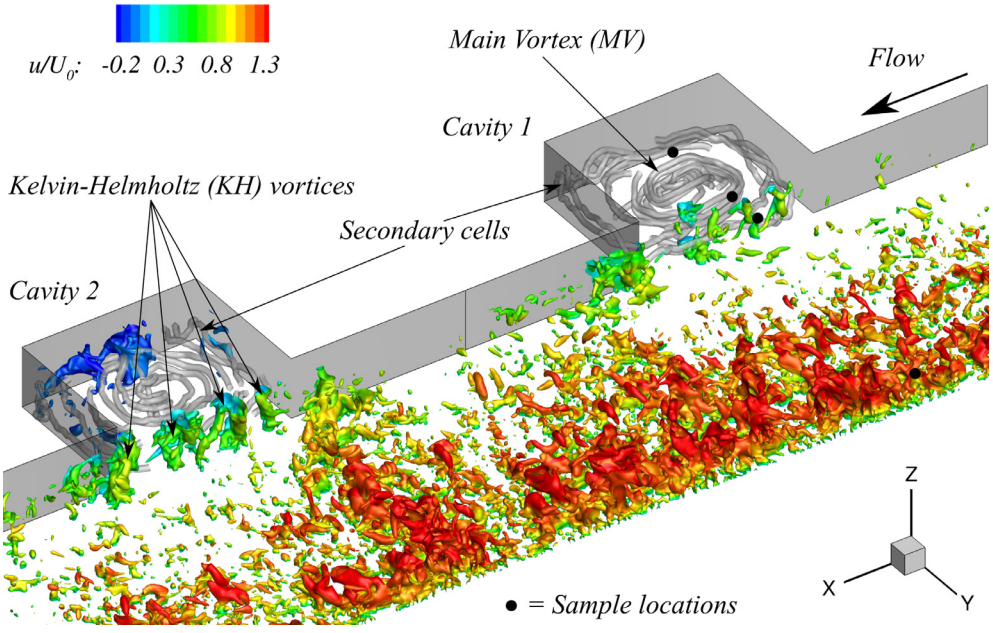


**Fig. 9.** Instantaneous flow structures represented with iso-surfaces of pressure fluctuation $p'$ coloured with normalised streamwise velocity for the case Q2. Only half of the channel width is displayed.

### 3.2. Instantaneous turbulent flow structures

The turbulent mechanisms of mass and momentum exchange between the main channel and the lateral cavities are conditioned by the coherent structures which form in the shear layer and penetrate inside the cavities.

Fig. 9 presents the turbulent structures deduced with iso-surfaces of instantaneous pressure fluctuation, $p' = p - P$, and coloured with streamwise velocity for half of the channel width for the case Q2. A broad spectrum of flow structures travelling through the main channel is observed with the largest ones advected along the middle of the main channel cross-section. Closer to the side walls the size of the turbulent structures reduces notably. Of great interest are the Kelvin-Helmholtz (KH) vortices developed in the shear layer at the mouth of the cavities as a consequence of the velocity difference between the low-velocity cavity flow and higher-velocities in the main stream. In their inherent 3D shape, KH vortices appear to keep a fairly coherent vertical structure across the water depth while convected downstream, as no large velocity gradients in the vertical direction are observed (Mignot et al., 2016). Such coherent shape is more consistent for case Q1 as the flow is shallower. Furthermore, the large-scale MVs occupy the entire embayments volume with vertically-evolving loci at relatively similar position over the cavity cross-section, as depicted in time-averaged streamlines in Fig. 4.

At the internal cavity corners secondary recirculating vortices are observed, which, as previously mentioned, are forced by continuity and by the shear between the MVs and sidewalls. Note that their size is considerably smaller than the MVs and, consequently, their influence in the hydrodynamics of the in-cavity flow, and the processes of exchange of mass and momentum between the cavity and the main channel, which are here under analysis, can be deemed negligible (Weitbrecht et al., 2008).

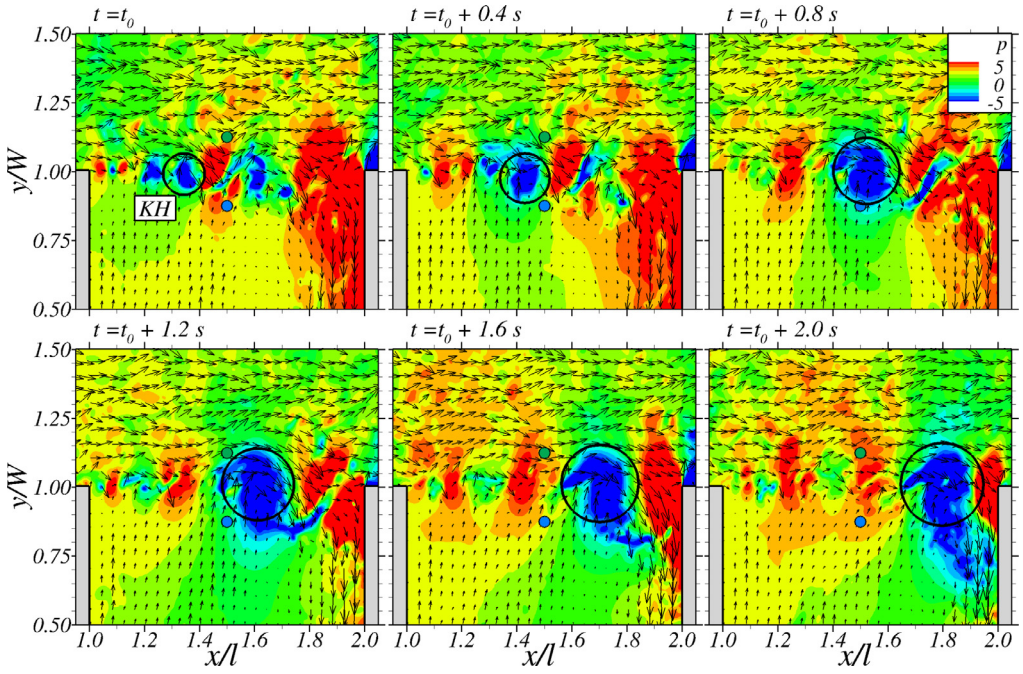


**Fig. 10.** Contours of instantaneous pressure, $p$, with velocity vectors of components $(0.2 \cdot u, v, 0)$ at a plane located at $z/h = 0.5$ for the flow conditions corresponding to the highest discharge, case Q3. The snapshots have a time lapse of 0.40 s among them.

Fig. 10 displays contours of instantaneous pressure, $p$, with vectors of 2D velocities with magnitudes $(0.2 \cdot u, v, 0)$ at a plane located at $z/h = 0.5$ for the flow conditions corresponding to the highest discharge, Q3, with a time lapse of 0.40 s between each consecutive snapshots. Here the two points located at $x/l = 1.5$ at $y/W = 0.875$ and 1.125 are included as they are used to collect pressure signal time series for the shear layer instability analysis in the spectral domain. At the upstream corner at $t = t_0$, the onset of the shear layer instabilities occurs as a result of the velocity gradients between regions (Mignot et al., 2016). In their early formation stages, the Kelvin-Helmholtz (KH) structures are relatively small but, as they are convected downstream, grow in size due to the interaction with the ambient flow and travel with an almost parallel direction to the cavity mouth transverse plane. For this reference cavity on the right-hand side of the main channel, KH vortices feature a clockwise rotation as a consequence of them being fed at their front edge by transversal velocities from the main channel moving into the cavity and at their trailing edge by those velocities being flushed out from the cavity. During the last stages of their downstream advection, KH vortices progressively loss coherence until impinging the downstream cavity corner, when they partially entrain into the cavity or continues with the main stream (Rockwell and Knisely, 1980). This is the main process of turbulent transport scalars between cavities and the main channel, as previously reported by Mignot et al., 2017 for square-like single cavity flows and Constantinescu et al., 2009 for scalar mixing in a series of groynes.

### 3.3. Spectral analysis of the variations in the pressure field

The results on the pressure field measured within the flow can reveal whether standing wave (SW) phenomena occur and whether there is a coherent pattern in the temporal generation of KH vortices travelling across the shear layer. As found in Wölfinger et al., 2012, when the frequency of the standing wave, $f_{SW}$ and that of the shear-layer vortex shedding $f_{SL}$ coincide, a lock-on phenomenon is experienced. Under these resonance conditions, the hydrodynamics of the in-cavity flow can dramatically change, modifying the mass and momentum exchanges between the main channel and cavities. Juez et al. (2018a) showed that under such conditions the in-cavity sedimentation processes can be also completely altered. The standing waves that appear in enclosed water domains are called seiches. Whilst $f_{SL}$ depends on the geometry of the cavity and flow conditions (Wölfinger et al., 2012), $f_{SW}$ can be approximated to be the eigenfrequency of the first eigenmode of the standing wave, $f_1$, determined as:

$$f_1 = \frac{\sqrt{gh}}{2B} \tag{4}$$

To quantify the differences in the variation of the pressure field at different locations in the transversal direction ($y$-direction), spectra of the pressure time-series, at the four sample locations located at $y/W = 0.125$, 0.875, 1.125 and 2.500 at mid water depth and depicted in Fig. 9, are computed and presented in Fig. 11. These locations are aligned with the cavity centre ($x/l = 1.5$) transverse to the main flow direction, as depicted in Fig. 10, allowing to determine the relevant oscillating phenomena conditioning in flow field.

At frequencies in inertial region and above, all the spectra feature two outstanding regions of slopes $-5/3$ and $-3$. These results suggest the existence of quasi-2D vortical structures that follow an inverse turbulent energy cascade (Nikora et al., 2007; Sommeria, 1986): energy transfer from the small eddies towards the large vortical structures is verified. Such turbulent dynamics corresponds to those observed in Fig. 10 in the shear layer region where small eddies are formed, advected downstream, and coalesce to form larger turbulent structures.

For high frequencies, in the region of the inverse cascade (with $-3$ slope) and regardless the flow conditions, the spectra at the four different transverse locations collapse with the same level of energy. However, for lower frequencies, the energy decay observed for the case Q1 is quite different between the points inside of the cavity, i.e. $y/W < 1.0$, and those outside. These observations for Q1, when compared with the cases Q2 and Q3, suggest that there is a separation between the turbulent dynamics between the inner and outer regions of the cavity for shallower flows. At the dissipative scales, when the flow tends to isotropy, this difference is no longer observed due to a similar spectral energy decay found in all cases.

Two notable peaks are always observed in the production range of the spectra presented. One corresponds to shedding frequency of the KH vortices produced in the shear layer region while a second energy peak

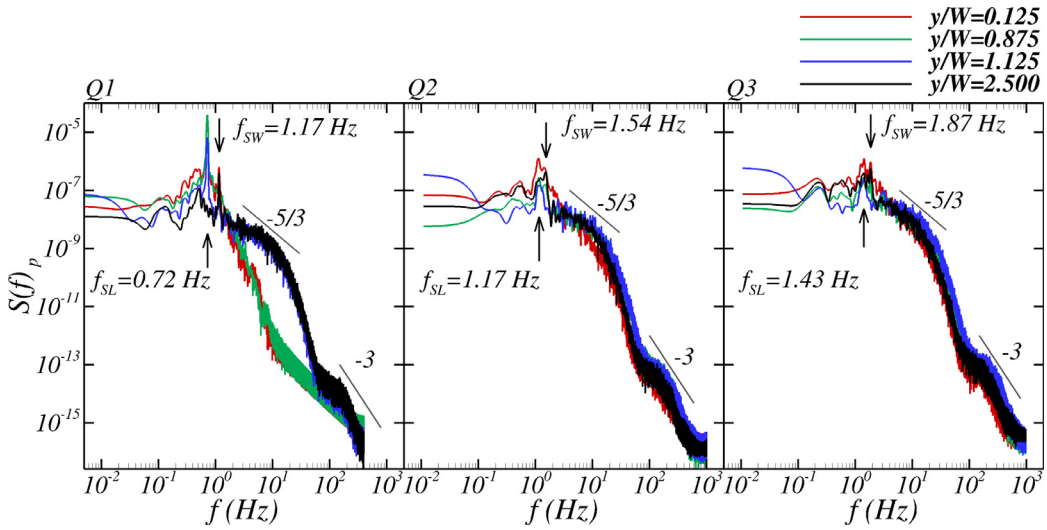


**Fig. 11.** Power spectral density computed from pressure time-series at four spatial samples located at different transverse locations and depicted in Fig. 9, for $x/l = 1.5$ and $z/h = 0.5$ (see Fig. 9) and for all the studied cases Q1, Q2 and Q3.

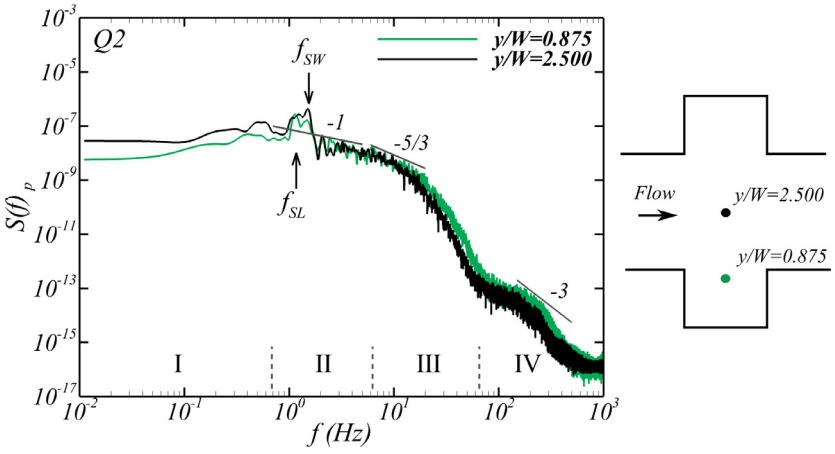


**Fig. 12.** Identification of the main ranges and slopes found in power spectral density computed from pressure time-series. Samples are located inside ($y/W = 0.875$) and outside ($y/W = 2.5$) of the cavity at $x/l = 1.5$ and $z/h = 0.5$, for the case Q2.

corresponds to the standing wave. For the case Q1, one of the peaks is common to the three positions inside and the verge of the cavity: $y/W =$ 0.125, 0.857 and 1.125. A second energy peak at higher frequency is observed for all the four positions, including $y/W = 2.500$, at the centre of the main channel. At the latter location, a signature from the KH vortices in the pressure signal is not expected according to the pressure field observed in Fig. 10. Hence, the first peak at lower frequency ($f_{SL}$) is attributed to the shear layer KH vortices shedding and the second peak at higher frequency ($f_{SW}$) to the standing wave which should be felt in the pressure field across the channel: $f_{SL} = 0.72$ Hz and $f_{SW} =$ 1.17 Hz respectively, for case Q1. For the cases Q2 and Q3, values of frequencies $f_{SL}$ and $f_{SW}$ increase with increasing flow rate and decreasing shallowness.

Frequencies $f_{SL}$ and $f_{SW}$ computed for the different cases are summarised in Table 3 together with values of $f_1$ (Eq. (4)). The ratio between $f_{SL}/f_{SW}$ are lower than the unity, although approaching this value with increasing flow rate, which suggests that both unsteady phenomena are not coupled, similar to the *pre lock-on* case in Wölfinger et al., 2012. For discharges higher than the ones tested, an interaction between the standing wave and shear-layer shedding is expected.

The ratio between the standing wave frequency from the numerical simulations ($f_{SW}$) with the theoretical standing-wave value ($f_1$) are close or above four, indicating that for all the studied cases no amplification of the effect of the standing wave due to resonance is expected, i.e. when

**Table 3**
Values of water depth, frequencies of shear layer vortex shedding ($f_{SL}$), standing wave ($f_{SW}$), approximated standing wave ($f_1$) and their ratio and reduced velocity ($U_r$) for the three cases. Values of the frequency of the shear layer ($f_{SL}$) and standing wave ($f_{SW}$) were obtained through the signal analysis displayed in Fig. 11. The value of the approximated standing wave ($f_1$) was computed by means of Eq. (4).

| Case | $h$ [m] | $f_{SW}$ [Hz] | $f_{SL}$ [Hz] | $f_1$ [Hz] | $f_{SL}/f_{SW}$ [-] | $f_{SW}/f_1$ [-] | $U_r$ [m/s] |
|---|---|---|---|---|---|---|---|
| Q1 | 0.035 | 1.17 | 0.72 | 0.29 | 0.61 | 3.99 | 0.76 |
| Q2 | 0.050 | 1.54 | 1.17 | 0.35 | 0.76 | 4.40 | 0.84 |
| Q3 | 0.070 | 1.87 | 1.43 | 0.41 | 0.77 | 4.51 | 0.86 |

$f_{SW} \approx f_1$. These results are confirmed with the lack of seiching observed during the experiments reported in (Juez et al., 2018c).

Finally, in Table 3 values of the reduced velocity, defined with the bulk velocity and main channel width as $U_r = U_0/(f_1 B)$, for the three cases Q1, Q2 and Q3 are presented. As $U_r$ is lower than the unity which again indicates non-resonance conditions are expected. In the experimental work by Wölfinger et al. (2012), for a single lateral cavity with similar Reynolds, Froude numbers and reduced frequency, analogous *pre lock-on* transient flow behaviour was found.

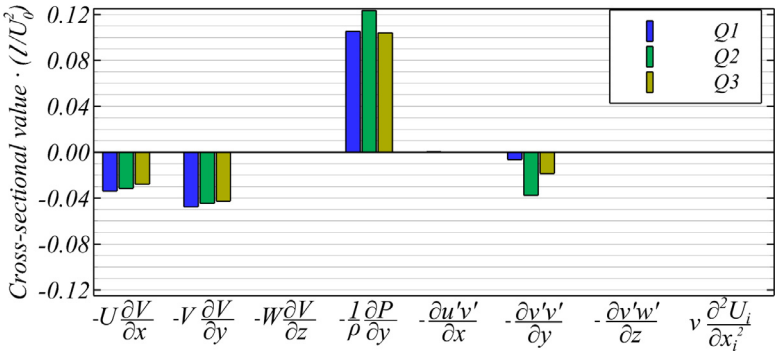


**Fig. 13.** Components of the terms of the *y*-RANS equation, spatially averaged over the mouth of the cavity plane, for the three cases Q1, Q2 and Q3.

Four ranges can be identified in the spectral distribution of the pressure signal, as depicted in Fig. 12 for Q2 at two sample locations, one inside the cavity and another in the main channel centreline. At the lowest frequencies, typically larger than the shear-layer shedding frequency, the energy production range "I" is found. The range "II" is characterised by an energy decay that follows a $-1$ slope, which was not drawn in Fig. 11 for clarity purposes. Nikora (1999) linked the $-1$ slope to the superposition of vortical structures in the energy cascade process. It is in this spectrum interval in which energy peaks at $f_{SL}$ and $f_{SW}$ are found. In the inertial sub-range "III", the energy decay follows the $-5/3$ slope as previously shown in Fig. 11. At frequencies in the order of $10^2$ Hz the dissipation range "IV" takes place, which features a $-3$ slope owed to the inverse cascade process commonly found in shallow flows. Kraichnan (1967) justified that both $-5/3$ and $-3$ slopes can be simultaneously present in the energy spectrum of two-dimensional flows, being the former a consequence of the largest flow scales transferring kinetic energy from low to high frequencies, whilst the latter is due to the small scales feeding the larger ones.

The intrinsic high-resolution of the simulations is evidenced thanks to the full palette of frequencies resolved. It is noteworthy that the present LES capture remarkably well the presence of the standing wave effect in the pressure field, despite adopting a rigid-lid approximation without explicitly resolving the free-surface motion. The sub-grid scale (sgs) model, responsible for taking into account the flow scales lower than the grid resolution, does not introduce any additional dissipation until frequencies in the order of $10^3$ Hz. This small interplay of the sgs model is also quantified with the ratio of the sgs to kinematic viscosity, which attains values lower than the unity in most of the computational domain.

### 3.4. Momentum transfer between main channel and lateral cavities

Governing processes in the momentum transfer between the main channel and lateral cavities are analysed looking at the components of the Reynolds Averaged Navier-Stokes (RANS) momentum equation in the spanwise direction (*y*-RANS), defined in Eq. (3). The embayments under analysis have a high aspect ratio, which means that the flow is expected to be of the skimming type as described by Meile et al., 2011. The aspect ratio corresponds to the case of the so-called "closed" cavity (Meile et al., 2011), in which the entrainment of main-channel streamwise momentum is limited, in opposition to what occurs in lower-aspect ratio geometries, i.e. with relatively larger cavity opening length.

The scale over which the terms in *y*-RANS equation are time-averaged is sufficiently large to ensure statistically convergence of second-order moments. This means that the instantaneous flow structures developed in the shear layer, said to be responsible for mass and momentum exchange (Weitbrecht et al., 2008; Constantinescu et al., 2009), are accounted within the turbulent stresses of the flow. Cross-sectional mean values of the *y*-RANS equation integrated over the mouth of the cavity plane are shown in Fig. 13 for the three cases normalised by $l/U_0^2$. Positive values indicate flush out of momentum whilst negative denote its entrainment into the cavity.

The results show that the pressure gradient is the only term responsible for driving the momentum out the cavity into the main channel for the present cases. On the other hand, terms involved in the entrainment of momentum from the main channel to the cavity are mainly the convection terms $U\partial V/\partial x$ and $V\partial V/\partial y$ and, to a lesser extent, the $v'v'$ Reynolds stress. The gradient of the turbulent momentum flux $u'v'$ has a negligible contribution to the transverse momentum exchange so does the viscous terms, as expected due to the high Reynolds number of the flow.

There is a similar pattern in the *y*-RANS results integrated over the mouth of the cavity for the three flow conditions. However, in the case Q2, there is a larger contribution from the pressure gradient counterbalanced by an additional larger gradient of turbulent flux $v'v'$, being the convection terms of the mean flow field very similar to those in Q1 and Q3. These results imply that the momentum exchange mechanisms vary depending on the flow conditions for the same cavity configuration. This agrees with the results on the sediment trapping efficiency obtained in the experimental work by Juez et al. (2018a). In their case, for the present high-aspect ratio geometry, the maximum efficiency was attained for Q2 and close values were obtained for Q1 and Q3, indicating a clear relation between momentum and sediment exchanges between the main channel and the cavities.

The distribution of the four main terms from the *y*-RANS equation across the mouth of the cavity is presented in Fig. 14 for the case Q2. It is observed that the convective term $-U\partial V/\partial x$ aids to momentum entrainment (negative values) in the 20% downstream part of the cavity whilst positive values are mostly found between $1.5 < x/l < 1.8$. The term $-V\partial V/\partial y$ features only two regions of large positive values, namely near the channel bottom and free-surface, indicating the regions where momentum is transported from the cavity to the main channel.

Near the downstream wall, the convective terms corresponding to the mean flow have large negative values and contribute to transverse momentum entrainment. The turbulent stress term, together with the convective ones, contribute to the net transport of spanwise momentum from the main channel into the cavity, and this is well-observed in its distribution over the mouth of the cavity which exhibits mostly negative values.

Finally, the pressure gradient contours in Fig. 14 show its positive contribution counterbalancing the turbulent term in the region $1.1 < x/l < 1.5$, and between $1.85 < x/l < 2.0$ the convective terms.

### 3.5. Mass exchange

Exchange of mass processes between the high-momentum main channel and lateral embayments vary depending on the geometric characteristics of the cavity. The present cavities feature an aspect ratio $W/l$ equal to 0.8 (i.e. skimming flow type) implying there is no entrainment of the main channel flow into the cavity. The exchange velocity $E$ across the channel-cavity interface is defined as the cross-sectional average value of the absolute transverse velocity, and the exchange coefficient $k$ relates the former exchange velocity with the bulk velocity, which read as:

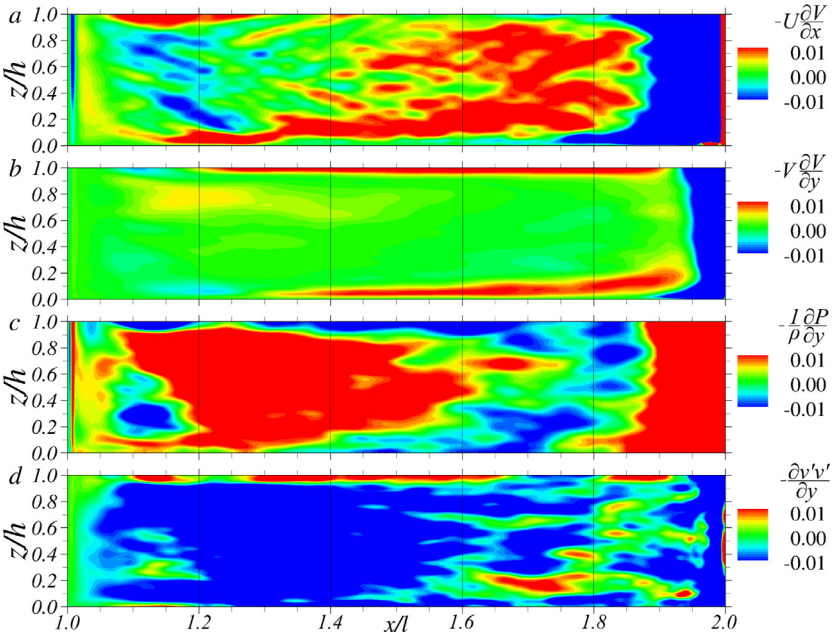


**Fig. 14.** Distribution along the cavity mouth of the main *y*-RANS equation components for the Q2 case.

**Table 4**
Values of the dimensionless exchange coefficient obtained during the experiments of Juez et al. (2018c) using PIV, and computed with LES using velocities across the cavity-opening plane and those at the free-surface.

| Case | $k$ (PIV) | $k$ (LES) | $k$ (LES-top) |
|---|---|---|---|
| Q1 | 0.043 | 0.0081 | 0.0145 |
| Q2 | 0.029 | 0.0090 | 0.0140 |
| Q3 | 0.015 | 0.0084 | 0.0147 |

$$E = \frac{1}{Wl}\int_0^l \int_0^W |V| dz dx \tag{5}$$

$$k = \frac{E}{2U_0} \tag{6}$$

Table 4 presents the exchange coefficient values, $k$, obtained in the experiments of Juez et al. (2018c), those computed from LES integrating across the mouth of the cavity at $y/W = 1.0$ (see Fig 6), and also those obtained from LES using the values of $|V|$ at the domain top lid. The latter values are calculated similarly to the experimental entrainment coefficients which were obtained by using PIV measurements at the water surface. The experimental and numerical entrainment coefficients differ notably, and only the $k$ values at LES-top display values with the same order of magnitude as the ones displayed in the laboratory. Disparity in the results of $k$ between experiments and numerical predictions have previously been reported by Constantinescu et al., 2009 in which $k$ was estimated from contaminant decay. Furthermore, $k$ values obtained with PIV decrease when the flow discharge increases (from Q1 to Q3). This agrees with Mignot et al., 2017 but not with the results reported in Weitbrecht et al., 2008. However, in Weitbrecht et al., 2008 seiching was not observed. Regarding the magnitude of the values, $k$ (PIV) and $k$ (LES-top) display similar values to those obtained in Weitbrecht et al., 2008; Mignot et al., 2017.

Despite the shallow nature of the flow, the turbulent structures that developed in the shear layer display 3D turbulent characteristics. Fig. 9 presents the turbulent structures plotted with iso-surfaces of pressure fluctuation. The turbulent structures in the vicinity of the shear layer are mainly contained within the main channel. The observed 3D turbulent structures behave as a vertical barrier avoiding the in-cavity development of the shear layer (McCoy et al., 2008). This is an important observation, since the mass exchange of fine sediments, pollutants or nutrients between the main channel and the cavities is thus notably limited/governed by the production of turbulence in this region of the channel.

During the experimental campaign carried out in Juez et al., 2018a plane view photos of the in-cavity sedimentation patterns were taken at the end of the experiment. These photos were treated to extract the surface occupied by the sediments. Fig. 15 presents iso-surfaces of time-averaged vertical velocities $W/U_0 = \pm 0.1$, contours of turbulent kinetic energy (*tke*) at $z/h = 0.01$, and areas corresponding to where sediments settled at the end of the experiments. Sediment deposition areas mostly coincide with those lacking large vertical velocities implying that near-bed vertical velocities are responsible for keeping them in suspension. Negative iso-surfaces of $W$ are found close to the lateral walls whilst positive values are mainly in the inner recirculation area. Additionally, deposition areas also seem to correlate with those where turbulent kinetic energy values are also small. These results indicate that sediment particles are able to settle when vertical velocities and turbulence are low.

## 4. Main Findings

The current research adopted high-resolution LES to identify and quantify the major role played by the vertical structures characteristic of in-cavity flows, specifically: vertically-oriented vortical elements generated in the shear layer; a main recirculating in-cavity vortex; and small-scale in-cavity vortices. Results of the hydrodynamics revealed that the flow within the cavities are reasonably shallow with their flow dynamics largely dominated by a large-scale structure, named as Main Vortex (MV), which extends over most of this confined region. The appearance of a single MV is due to the relatively squared shape of the cavities, resembling to a skimming flow type in which the entrainment of momentum from the main stream into the macro-roughness elements is reduced. While this energetic flow structure is expected to feature a quasi-2D shape owed to the shallow flow conditions, the vertical position of its core is proven to vary with depth, especially for the deeper case. It is closer to the opening of the cavities near the bottom, whilst moving towards to the opposite wall at the free-surface.

The velocity differences in the transition between the high-momentum main channel and low-velocity cavities leads to the for-

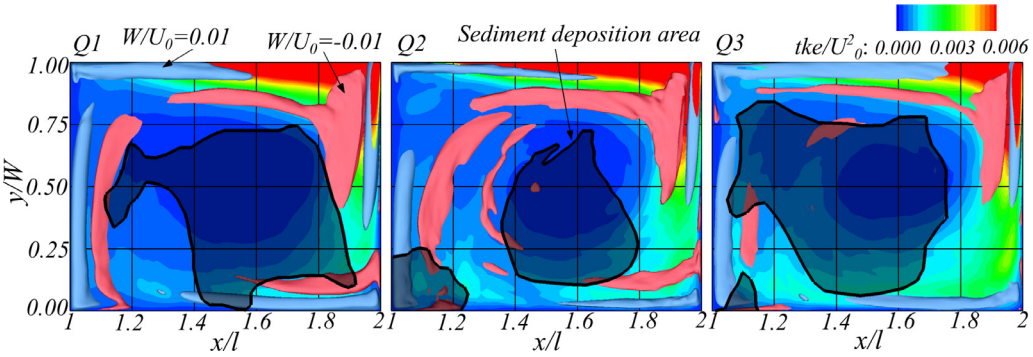


**Fig. 15.** Comparison of the sediment deposition regions (shaded areas) obtained during the experimental campaign (Juez et al., 2018a) with the computed flow field near the bottom bed of the cavity. Contours of turbulent kinetic energy are at $z/h = 0.01$ and iso-surfaces of vertical velocities show values $W/U_0 = \pm 0.1$. Note that only velocity iso-surfaces at $z = 7$ mm and below are shown.

mation of shear layers, in which a train of coherent vortices develops due to Kelvin-Helmholtz (KH) instability. In spite of the shallow nature of the flow, these structures feature a 3D nature occupying the whole water column (see Fig. 9). These KH vortices are smaller than the MV and travel over the mouth of the cavity plane affecting both the in-cavity flow and the adjacent main channel region. During their convection, they increase in size while remaining coherent until impinging the downstream cavity wall (Figs. 9 and 10). A fairly uniform distribution of the Reynolds stresses over the whole water depth and across the channel-cavity transition is also observed due to this coherence. At the last stage, when impinging the downstream corner of the cavity, the KH vortices breakdown, partially entraining into the cavity or going away with the main stream.

As a result of this activity and dominance of the KH vortices, the mass exchange between the main stream and in-cavity flow is limited and, consequently, the dimensionless exchange coefficients computed with LES are lower than the ones obtained with the surface PIV (see Table 4). LES results show the largest transverse velocities across the mouth of the cavity are found in mainly two pockets extending across most of the streamwise length of the embayment but confined at vertical locations near the free-surface and bottom bed (Fig. 6). Such velocity distribution highlights that the mass exchange between the main channel and cavities is largely heterogeneous. Hence, it is therefore inaccurate to assume that the flow patterns observed at the water surface can precisely determine the mass exchange between the main flow and lateral embayments.

LES captures recurrent temporal oscillations in the pressure fluctuations across the entire channel, despite a shear-free rigid-lid condition is imposed at the free-surface. At several sample locations distributed across the channel width, a peak in the spectral energy distribution of the pressure signal is observed at frequencies close to those of the theoretical standing wave. In addition, spectra inside of the cavity revealed that shear-layer phenomena affect the dynamics of the in-cavity flow and adjacent region of the main channel, which was observed in the pathway of KH vortices during their advection (Fig. 10). The spectral analysis also reveals that the energy of the quasi-2D MV is fed by the smaller scale structures from the shear layer, observed in the $-3$ slope of the spectra in the dissipation range. Conversely, the energy decay of the largest flow structures follows a $-1$ slope until the inertial sub-range is reached.

The momentum transfer between the main channel and cavities is analysed with the Reynolds Averaged momentum equation in the cross-flow direction. The integration of each of the involved terms across the main channel-cavity transition plane reveals a large impact of the pressure gradient in the transverse momentum exchange. This appears to be the sole responsible for the momentum flush-out from the cavities to the main stream, mostly counterbalanced by the convective terms with a reduced contribution of the Reynolds normal stresses. Such key role of the pressure field in the momentum balance together with the fact that the shedding frequency of shear-layer KH vortices is nearly coupled with the standing-wave frequency, can be linked to the relevance of the seiche phenomenon in the sediment transport.

The turbulent flow characteristics computed inside the cavities served as a proxy to determine the sediment exchange reported in the laboratory experiments in Juez et al., 2018a. The LES-predicted patterns of iso-surfaces of vertical velocities are linked to pathways of sediment movement: sediment deposition areas are bounded by regions in which vertical velocities are lower than 1% the bulk velocity and levels of turbulent kinetic energy are low. These findings reflect that the ease of the sediments to deposit within the cavity relies on the secondary flow distribution and its unsteadiness.

A key finding from this study is that low-frequency transverse pressure changes arises as an essential factor in the sediment transport in river bank lateral cavity flows. This variable is normally absent in experimental tests with PIV or ADV and normally omitted in the analysis. Such importance becomes crucial to understand why sediment transport dynamics change when seiching is present (Tuna et al., 2013). This, combined with the coupling of the standing wave and shear-layer KH vortices shedding that can further amplify the pressure field oscillations, determine when a given lateral embayment geometry performs best to trap sediments from the main channel, as previously observed in experimental tests in Juez et al., 2018a.

Establishing the link between flow and sediment transport is crucial in understanding the geomorphological evolution of the lateral embayments. The information related to the accurate quantification of the mass exchange between the main channel and the lateral embayments may be used for the application of measures against sedimentation problems or to identify the magnitude and sources of pollutants, nutrients and carbon, which are fixed to and conveyed with the sediment. For example, the impact of the release of fine sediments by reservoir flushing operations on the in-cavity sedimentation could be better assessed by knowing the interaction between the flow rates and the geometry of lateral embayments. The long-term maintenance of the cavities could thus be guaranteed. Furthermore, as future work the additional modelling of the sediment particles in suspension will be considered in the LES model to account for their impact on the bulk flow.

## 5. Conclusions

The main drivers in the mass and momentum exchange between the main channel and symmetrically-distributed river lateral cavity have been identified via large-eddy simulations (LES). Three cases with varying shallowness and flow discharge were analysed for a single embayment geometry. Despite the relatively shallow nature of the flow, the hydrodynamics notably changed for each flow condition, all of which proved to be highly three-dimensional both across the main channel, within the cavities and also in their transition region. In order to elucidate and quantify such complex flow nature, high-resolution LES were

carried out to complement the experimental observations so as to understand the driving mechanisms also involved in sediment transport.

Regarding mass exchange, this study outlines that large streamwise and transversal velocities were mostly found in regions near the bottom and top lids over the mouth of the cavities. A single main vortex occupied most of the volume of each cavity, being the location of its core not uniformly distributed over the water depth. LES captured the dominant Kelvin-Helmholtz flow structures generated and convected over the shear layers developed in the channel-cavity transition. Despite a rigid-lid was adopted to represent the free-surface, LES captured well the standing wave phenomenon originated from pressure field oscillations. This was identified from pressure spectra at various locations across the channel width. Peaks in the spectral energy due to the shear-layer vortices shedding were also observed but only at those locations within or close to the lateral cavities.

The areas of sediment deposition obtained during a previous experimental campaign agreed well with areas of low turbulence and vertical velocities predicted by the LES near the embayments bottom. This study quantified that the gradient of pressure is the main responsible for the transport of transverse momentum out of the cavity, counterbalanced by inwards transport due to convection and Reynolds normal stresses. The identification of the main mechanisms developed in the channel-cavity transition provides new insights into the sediment exchange and deposition processes.

## Declaration of Competing Interest

The authors declare that they have no known competing financial interests or personal relationships that could have appeared to influence the work reported in this paper.

## CRediT authorship contribution statement

**Pablo Ouro:** Data curation, Formal analysis. **Carmelo Juez:** Writing - original draft. **Mário Franca:** Conceptualization, Writing - review & editing.

## Acknowledgements

The authors would like to acknowledge the support of the Supercomputing Wales project, which is partially funded by the European Regional Development Fund (ERDF) via the Welsh Government. Furthermore, the second author, Carmelo Juez, is funded by the H2020-MSCA-IF-2018 programme (Marie Sklodowska-Curie Actions) of the European Union under REA grant agreement (number 834329-SEDILAND).

## References

Akutina, Y., 2015. Experimental Investigation of Flow Structures in a Shallow Embayment Using 3D-PTV. McGill University, Montréal Ph.D. thesis.

van Balen, W., Blankaert, K., Uijttewaal, W., 2010. Analysis of the role of turbulence in curved open-channel flow at different water depths by means of experiments, LES and RANS. J. Turbul. 11 (12), 1–34.

Bomminayuni, S., Stoesser, T., 2011. Turbulence statistics in an open-channel flow over a rough bed. J. Hydraul. Eng. 137 (11), 1347–1358.

Cevheri, M., McSherry, R., Stoesser, T., 2016. A local mesh refinement approach for large-eddy simulations of turbulent flows. Int. J. Numer. MethodsFluids 82, 261–285.

Constantinescu, G., Sukhodolov, A., McCoy, A., 2009. Mass exchange in a shallow channel flow with a series of groynes: LES study and comparison with laboratory and field experiments. Environ. Fluid Mech. 9, 587–615. https://doi.org/10.1007/s10652-009-9155-2.

Fang, H., Bai, J., He, G., Zhao, H., 2014. Calculations of nonsubmerged groin flow in a shallow open channel by large-eddy simulation. J. Eng. Mech. 140, 04014016. https://doi.org/10.1061/(ASCE)EM.1943-7889.0000711.

Federal Office of Environment, 2016. Hydrological data service for watercourses and lakes. URL http://www.bafu.admin.ch/wasser

Gualtieri, C., 2008. Numerical simulation of flow patterns and mass exchange processes in dead zones. 4th International Congress on Environmental Modelling and Software, Barcelona, Spain.

Jackson, T.R., Haggerty, R., Apte, S.V., Coleman, A., Drost, K.J., 2012. Defining and measuring the mean residence time of lateral surface transient storage zones in small streams. Water Resour. Res. 48 (10). https://doi.org/10.1029/2012WR012096.

Jackson, T.R., Haggerty, R., Apte, S.V., O'Connor, B.L., 2013. A mean residence time relationship for lateral cavities in gravel-bed rivers and streams: incorporating streambed roughness and cavity shape. Water Resour. Res. 49 (6), 3642–3650. https://doi.org/10.1002/wrcr.20272.

Juez, C., Buhlmann, I., Maechler, G., Schleiss, A.J., Franca, M.J., 2018a. Transport of suspended sediments under the influence of bank macro-roughness. Earth Surf. Process. Landforms 43, 271–284. https://doi.org/10.1002/esp.4243.

Juez, C., Hassan, M.H., Franca, M.J., 2018b. The origin of fine sediment determines the observations of suspended sediment fluxes under unsteady flow conditions. Water Resour. Res. 54, 5654–5669. https://doi.org/10.1029/2018WR022982.

Juez, C., Murillo, J., García-Navarro, P., 2014. A 2D weakly-coupled and efficient numerical model for transient shallow flow and movable bed. Adv. Water Resour. 71, 93–109. https://doi.org/10.1029/2018WR022982.

Juez, C., Thalmann, M., Schleiss, A.J., Franca, M.J., 2018c. Morphological resilience to flow fluctuations of fine sediment deposits in bank lateral cavities. Adv. Water Resour. 115, 44–59. https://doi.org/10.1016/j.advwatres.2018.03.004.

Kähler, C.J., Scharnowski, S., Cierpka, C., 2012. On the uncertainty of digital PIV and PTV near walls. Exp. Fluids 52 (6), 1641–1656. https://doi.org/10.1007/s00348-012-1307-3.

Kemp, P., Sear, D., Collins, A., Naden, P., Jones, I., 2011. The impacts of fine sediment on riverine fish. Hydrol. Processes 25, 1800–1821. https://doi.org/10.1002/hyp.7940l.

Kimura, I., Hosoda, T., 1997. Fundamental properties of flows in open channels with dead zone. J. Hydraul. Eng. 123 (2), 98–107.

Koken, M., Constanstinescu, G., 2009. An investigation of the dynamics of coherent structures in a turbulent channel flow with a vertical sidewall obstruction. Phys. Fluids 21 (8), 85104. https://doi.org/10.1063/1.3207859.

Kraichnan, R., 1967. Inertial ranges in two-dimensional turbulence. Phys. Fluids 10, 1417. https://doi.org/10.1017/S0022112086000836.

Langendoen, E., Kranenburg, C., Booij, R., 1994. Flow patterns and exchange of matter in tidal harbours. J. Hydraul. Res. 32, 259–270.

Lesack, L.F.W., Marsh, P., 2010. River-to-lake connectivities, water renewal, and aquatic habitat diversity in the Mackenzie river delta. Water Resour. Res. 46 (12). https://doi.org/10.1029/2010WR009607.

Liu, Y., Stoesser, T., Fang, H., Papanicolau, A., Tsakiris, A., 2017. Turbulent flow over an array of boulders placed on a rough permeable bed. Comput. Fluids 158, 120–132.

McCoy, A., Constantinescu, G., Weber, L.J., 2006. Exchange processes in a channel with two vertical emerged obstructions. Flow Turbul. Combust. 77, 97–126. https://doi.org/10.1007/s10494-006-9039-1.

McCoy, A., Constantinescu, G., Weber, L.J., 2008. Numerical investigation of flow hydrodynamics in a channel with a series of groynes. J. Hydraul. Eng. 134 (2), 157–172. https://doi.org/10.1061/(ASCE)0733-9429.2008134:2.157.

Meile, T., Boillat, J.-L., Schleiss, A.J., 2011. Flow resistance caused by large-scale bank roughness in a channel. J. Hydraul. Eng. 137 (12), 1588–1597. https://doi.org/10.1061/(ASCE)HY.1943-7900.0000469.

Mignot, E., Cai, W., Launay, G., Riviere, N., Escauriaza, C., 2016. Coherent turbulent structures at the mixing-interface of a square open-channel lateral cavity. Phys. Fluids 25, 45104. https://doi.org/10.1063/1.4945264.

Mignot, E., Cai, W., Polanco, J.I., Escauriaza, C., Riviere, N., 2017. Measurement of mass exchange processes and coefficients in a simplified open-channel lateral cavity connected to a main stream. Environ. Fluid Mech. 17, 429–448. https://doi.org/10.1007/s10652-016-9495-7.

Navas-Montilla, A., Juez, C., Franca, M., Murillo, J., 2019. Depth-averaged unsteady RANS simulation of resonant shallow flows in lateral cavities using augmented WENO-ADER schemes. J. Comput. Phys. 395, 511–536. https://doi.org/10.1016/j.jcp.2019.06.037.

Navas-Montilla, A., Murillo, J., 2016. Asymptotically and exactly energy balanced augmented flux-ADER schemes with application to hyperbolic conservation laws with geometric source terms. J. Comput. Phys. 317, 108–147. https://doi.org/10.1016/j.jcp.2016.04.047.

Nezu, I., Onitsuka, K., 2002. PIV measurements of side-cavity open-channel flows. Wando model in rivers. J. Vis. 5, 77–84.

Nicoud, F., Ducros, F., 1999. Subgrid-scale stress modelling based on the square of the velocity gradient tensor. Flow Turbul. Combust. 62, 183–200. https://doi.org/10.1023/A:1009995426001.

Nikora, V., 1999. Origin of the "21" spectral law in wall-bounded turbulence. Phys. Rev. Lett. 83, 734. https://doi.org/10.1103/PhysRevLett.83.734.

Nikora, V., Goring, D., 2002. Fluctuations of suspended sediment concentration and turbulent sediment fluxes in an open-channel flow. J. Hydraul. Eng. 128 (2), 214–224.

Nikora, V., Nokes, R., Veale, W., Davidson, M., Jirka, G.H., 2007. Large-scale turbulent structure of uniform shallow free-surface flows. Environ. Fluid Mech. 7, 159–172. https://doi.org/10.1007/s10652-007-9021-z.

Ouro, P., Fraga, B., Lopez-Novoa, U., Stoesser, T., 2019. Scalability of an Eulerian-Lagrangian large-eddy simulation solver with hybrid MPI/OpenMP parallelisation. Comput. Fluids 179, 123–136. https://doi.org/10.1016/j.compfluid.2018.10.013.

Ouro, P., Fraga, B., Viti, N., Angeloudis, A., Stoesser, T., Gualtieri, C., 2018a. Instantaneous transport of a passive scalar in a turbulent separated flow. Environ. Fluid Mech. 18 (2), 487–513. https://doi.org/10.1007/s10652-017-9567-3.

Ouro, P., Stoesser, T., Fraga, B., Lopez-Novoa, U., 2018b. Hydro3D repository. 10.5281/zenodo.1200187.

Ouro, P., Wilson, C.A.M.E., Evans, P., Angeloudis, A., 2017. Large-eddy simulation of shallow turbulent wakes behind a conical island. Phys. Fluids 29 (12), 126601. https://doi.org/10.1063/1.5004028.

Ribi, J., Boillat, J., Peter, A., Schleiss, A.J., 2014. Attractiveness of a lateral shelter in a channel as a refuge for juvenile brown trout during hydropeaking. Aquat. Sci. 76, 527–541. https://doi.org/10.1007/s00027-014-0351-x.

Rockwell, D., Knisely, C., 1980. Observations of the three-dimensional nature of unstable flow past a cavity. Phys. Fluids 23, 425. https://doi.org/10.1063/1.863009.

Rodi, W., Constantinescu, G., Stoesser, T., 2013. Large-Eddy Simulation in Hydraulics. CRC Press.

Sanjou, M., Nezu, I., 2013. Hydrodynamic characteristics and related mass-transfer properties in open-channel flows with rectangular embayment zone. Environ. Fluid Mech. 13, 527–555. https://doi.org/10.1007/s10652-013-9279-2.

Sanjou, M., Okamoto, T., Nezu, I., 2018. Dissolved oxygen transfer into a square embayment connected to an open-channel flow. Int. J. Heat Mass Transf. 125, 1169–1180. https://doi.org/10.1016/j.ijheatmasstransfer.2018.04.107.

van Schijndel, S.A.H., Kranenburg, C., 1998. Reducing the siltation of a river harbour. J. Hydraul. Res. 36, 803–814.

Sommeria, J., 1986. Experimental study of the two-dimensional inverse energy cascade in a square box. J. Fluid Mech. 170, 139–168. https://doi.org/10.1017/S0022112086000836.

Stoesser, T., 2010. Physically realistic roughness closure scheme to simulate turbulent channel flow over rough beds within the framework of LES. J. Hydraul. Eng. 136, 812–819. https://doi.org/10.1061/(ASCE)HY.1943-7900.0000236.

Stoesser, T., Braun, C., García-Villalba, M., Rodi, W., 2008. Turbulence structures in flow over two-dimensional dunes. J. Hydraul. Eng. 134 (1), 42–55. https://doi.org/10.1061/(ASCE)0733-9429(2008)134:1(42).

Sukhodolov, A., 2014. Hydrodynamics of groyne fields in a straight river reach: insight from field experiments. J. Hydraul. Res. 52(1), 105–120. https://doi.org/10.1080/00221686.2014.880859.

Thorel, M., Piégay, H., Barthelemy, C., Räpple, B., Gruel, C.-R., Marmonier, P., Winiarski, T., Bedell, J.-P., Arnaud, F., Roux, G., Stella, J.C., Seignemartin, G., Tena-Pagan, A., Wawrzyniak, V., Roux-Michollet, D., Oursel, B., Fayolle, S., Bertrand, C., Franquet, E., 2018. Socio-environmental implications of process-based restoration strategies in large rivers: should we remove novel ecosystems along the Rhône (France)? Reg. Environ. Change 18 (7), 2019–2031. https://doi.org/10.1007/s10113-018-1325-7.

Tuna, B.A., Tinar, E., Rockwell, D., 2013. Shallow flow past a cavity: globally coupled oscillations as a function of depth. Exp. Fluids 54, 1586. https://doi.org/10.1007/s00348-013-1586-3.

Uijttewaal, W.S.J., Lehmann, D., van Mazijk, A., 2001. Exchange processes between a river and its groyne fields: model experiments. J. Hydraul. Eng. 127 (11), 157–172.

Uno, K., Kazuuma, N., Tsujimoto, G., Kakinoki, T., 2013. Trapping effect of fine sediment in wand. J. Jpn. Soc. Civ. Eng. Ser. B3 69, 922–927.

Valentine, E.M., Wood, I.R., 1979. Experiments in longitudinal dispersion with dead zones. J. Hydraul. Div. 105(HY8), 999–1016.

Weitbrecht, V., Socofolosky, S.A., Jirka, G.H., 2008. Experiments on mass exchange between groin fields and main stream in rivers. J. Hydraul. Eng. 134 (2), 173–183. https://doi.org/10.1061/(ASCE)0733-9429(2008)134:2(173).

Wölfinger, M., Ozen, C.A., Rockwell, D., 2012. Shallow flow past a cavity: coupling with a standing gravity wave. Phys. Fluids 24, 104103. https://doi.org/10.1063/1.4761829.

Wood, P., Armitage, P., 1997. Biological effects of fine sediment in the lotic environment. Environ. Manage. 21 (2), 203–217. https://doi.org/10.1007/s002679900019.